THE JOURNAL OF PHYSICAL CHEMISTRY B

Article

pubs.acs.org/JPCB

Probing the Catalytic Mechanism Involved in the Isocitrate Lyase Superfamily: Hybrid Quantum Mechanical/Molecular Mechanical Calculations on 2,3-Dimethylmalate Lyase

Nathjanan Jongkon,[†] Warot Chotpatiwetchkul,[‡] and M. Paul Gleeson*[,‡]

[†]Department of Social and Applied Science, College of Industrial Technology, King Mongkut's University of Technology, North Bangkok, Bangkok 10800, Thailand

[‡]Department of Chemistry, Faculty of Science, Kasetsart University, Chatuchak, Bangkok 10903, Thailand

Supporting Information

ABSTRACT: The isocitrate lyase (ICL) superfamily catalyzes the cleavage of the C(2)−C(3) bond of various α-hydroxy acid substrates. Members of the family are found in bacteria, fungi, and plants and include ICL itself, oxaloacetate hydrolase (OAH), 2-methylisocitrate lyase (MICL), and (2*R*,3*S*)-dimethylmalate lyase (DMML) among others. ICL and related targets have been the focus of recent studies to treat bacterial and fungal infections, including tuberculosis. The catalytic process by which this family achieves C(2)−C(3) bond breaking is still not clear. Extensive structural studies have been performed on this family, leading to a number of plausible proposals for the catalytic mechanism. In this paper, we have applied quantum mechanical/molecular mechanical (QM/MM) methods to the most recently reported family member, DMML, to assess whether any of the mechanistic proposals offers a clear energetic advantage over the others. Our results suggest that Arg161 is the general base in the reaction and Cys124 is the general acid, giving rise to a rate-determining barrier of approximately 10 kcal/mol.

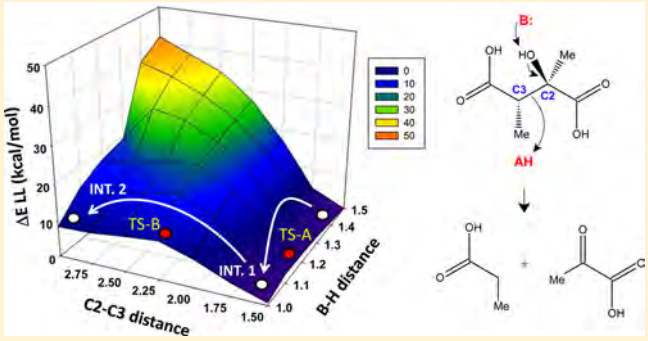

1. INTRODUCTION

The isocitrate lyase (ICL)/phosphoenolpyruvate mutase (PEPM) superfamily is a collection of proteins with high structural similarity that are involved in critical metabolic events.[1−7] Members of the lyase branch of the family, which includes ICL, 2-methylisocitrate lyase (MICL), oxaloacetate hydrolase (OAH), (2*R*,3*S*)-dimethylmalate lyase (DMML), and petal death protein (PDP), play roles in important metabolic processes including the citric acid, methylcitric acid, and glyoxylate cycles. Furthermore, recent research suggests that inhibition of these metabolic cycles could be a potentially novel route to treat bacterial and fungal infections,[8] including tuberculosis.[9,10]

The ICL/PEPM members adopt a distorted α/β-barrel tertiary structure in which seven of the eight helices pack up against the eight-stranded parallel β-sheet.[1−3,11−18] In both subclasses, metal cofactors play important mechanistic roles in conjunction with conserved Arg and Cys residues, as well as other polar residues.[1,2,11−14] Mechanistic proposals for the ICL branch of the superfamily have been made thus far from experimental data; however, the precise residues involved and the sequence of events are still not resolved.[1,11−15] It is generally believed that the process involves deprotonation of the substrate C2-OH group and formation of a carbonyl leading to the breaking of the C(2)−C(3) bond, followed by protonation of the carbanion that develops at the C(3) position.[11] However, the identity of the general base and acid in the process and the precise sequence of events remain unresolved.

DMML is a member of the ICL branch of the superfamily, which is widely distributed among microorganisms including bacteria such as *Aspergillus niger*,[1] *Eubacterium barkeri*,[4] and *Clostridium barkeri*.[6] DMML catalyzes cleavage of the C(2)−C(3) bond of its substrate, (2*R*,3*S*)-dimethylmalate (DMM), leading to the formation of dicarboxylate products propionate and pyruvate as shown in Scheme 1.[1,4−7] Furthermore, Narayan et al.[1] have studied the biochemical properties, substrate selectivities, and active-site characteristics of DMML in great detail. They reported a crystal structure containing a natural substrate mimic bound to the active site in a catalytically relevant conformation. The active site of metal-dependent DMML enzyme contains a Mn^{2+} cofactor in an octahedral configuration, coordinated to three water molecules, the acidic side chain of Asp87, and the bound ligand through two oxygen-mediated interactions.[1,11] Two distinct proposals have been put forward regarding the mechanism of DMML and other ICL

Received: May 18, 2015
Revised: July 27, 2015
Published: July 29, 2015

DOI: 10.1021/acs.jpcb.5b04732
J. Phys. Chem. B 2015, 119, 11473−11484

Scheme 1. Proposed Mechanisms for Catalytic Conversion of (2*R*,3*S*)-Dimethylmalate to Propionate and Pyruvate by DMML[a]

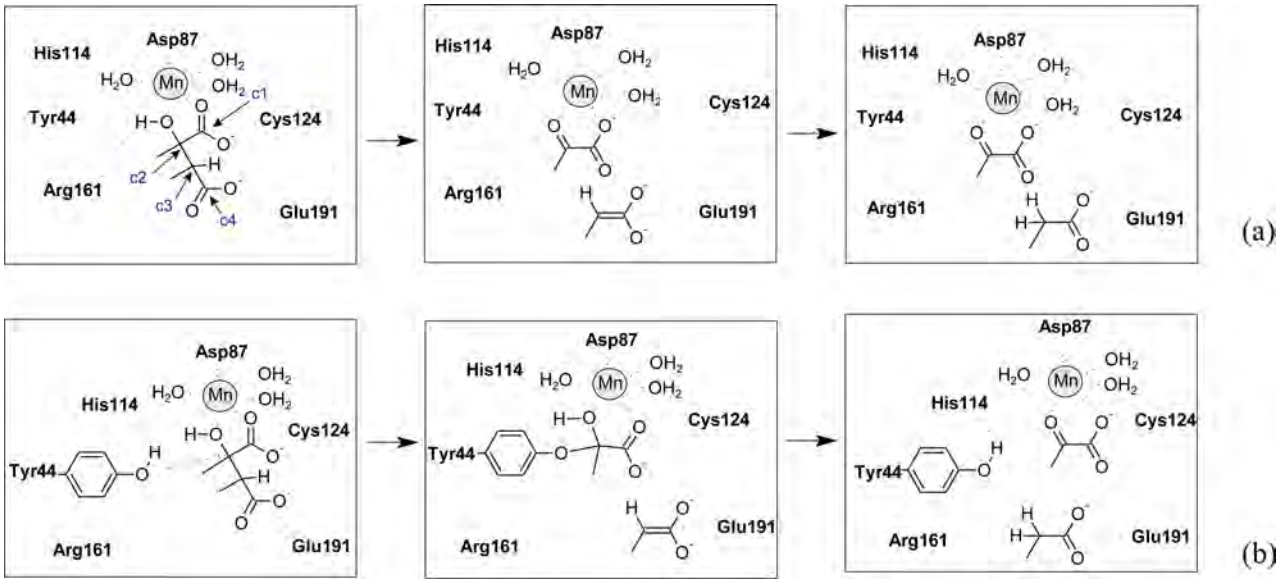

[a]Proposed to occur via (a) an acid/base-catalyzed process and (b) a nucleophile-assisted process.

family members.[1,2,11] The first mechanism requires the generation of an oxyanion at the C2 position through proton transfer to a base whose identity is not clear (possibilities include the conserved Arg161 or a Mn^{2+}-bound water molecule). Proton transfer results in the formation of a carbonyl at C2 followed by C(2)−C(3) bond breakage, thereby leading to formation of an anionic intermediate. This species can be protonated by an acid whose identity could be Cys124 or a Mn^{2+}-bound water molecule, or perhaps Glu191 or Asp87 (by proton shuttling via Mn^{2+}-bound water).[1,11] A second mechanism was initially proposed for the related ICL/MICL[11] before being extended to DMML.[1] This mechanism involves the generation of a Tyr44 nucleophile though transfer of a proton to His114, which in turn is stabilized by the amide carbonyl of Asp87 (i.e., a form of catalytic triad).[11,19]

Computational approaches can play a significant role in studying catalytic mechanisms.[20−22] In particular, the combined quantum mechanics and molecular mechanics (QM/MM) approach has been used to gain insight into the catalytic mechanisms at the sites where the chemical reactions take place.[22−26] In this method the active-site region is modeled by QM and the surrounding protein and solvent are treated with less computationally demanding MM. The method has been used in the past to study drug metabolism at cytochrome P450s,[27] to investigate suicide inhibitors,[28,29] and indeed to re-evaluate mechanisms of well-known proteins.[30] To date no theoretical mechanistic analysis has been performed on lyases of the ICL class. Nevertheless, interest in lyases has increased recently, with QM/MM studies being reported by Zhang and Liu[31] on aspartate ammonia lyase, Daniels et al.[32] on *N*-acetylneuraminic acid lyase, Su et al.[33] on α-1,4-glucan lyase, and Zhu et al.[34] on (*R*)-hydroxynitrile lyases. While the chemistry and active sites differ markedly, it is interesting to note the involvement of a catalytic triad in (*R*)-hydroxynitrile lyases and a Tyr acid/base in *N*-acetylneuraminic acid lyase. Furthermore, QM/MM calculations on citrate synthase[35] show that Arg[36] could also be a possible candidate as the general base in DMML, while studies on pyruvate formate lyase[37] also confirm the catalytic potential of Cys residues.

We report herein QM/MM studies aimed at improving our understanding of the catalytic events that take place within DMML and, by extension, the structurally and biochemically related proteins ICL, MICL, and PDP. To this end we have generated density functional theory (DFT)/AMBER QM/MM models to explore the two main mechanistic proposals put forward on the basis of experimental structural data, while we also try to identify which are the most likely acidic and basic residues involved in each scenario. Shedding light on the mechanistic processes at work within this family may open up opportunities to modulate its activity. Mechanistic knowledge has proved useful in development of transition-state analogue inhibitors for neuraminidase,[38] while recent literature proposes that efforts to develop covalent inhibitors should be increased.[39−41] In the latter case, a detailed understanding of the catalytic mechanism of proteins means that specific covalent strategies can be implemented that exploit the proteins' intrinsic reactivity. Indeed, Sharma et al.[16] note that inhibition of ICL by 3-bromopyruvate is accomplished via dehalogenation of the inhibitor to form a covalent adduct with the active-site nucleophile Cys191.

2. METHODS

An X-ray crystal structure of DMML containing a natural substrate mimic (PDB entry 3FA3)[1] was downloaded from the Research Collaboratory for Structural Bioinformatics (RCSB) data bank. The 3,3-difluorooxaloacetate substrate bound in the active site was used to construct the natural substrate [(2*R*,3*S*)-dimethylmalate, DMM] in its *gem*-diol form.[15] Missing atoms were added by use of Discovery Studio 4.1 (Accelrys Inc., San Diego, CA). The protonation states of amino acids were set by use of information derived from the PROPKA program[42−44] and based on a visual assessment of the environment of the residues in question. Histidine residues in the protein were set as HID, except for His55 (HIP) and His126 (HIE). Glu191 was set in the neutral form due to the short distance between the carboxylate of DMM, which indicates one of the acid moieties is protonated. The very short interatomic distance between Arg161 and the metal-bound hydroxyl group of DMM

DOI: 10.1021/acs.jpcb.5b04732
J. Phys. Chem. B 2015, 119, 11473−11484

Scheme 2. QM/MM Stationary Points Obtained in This Study for Conversion of DMM to Propionate and Pyruvate

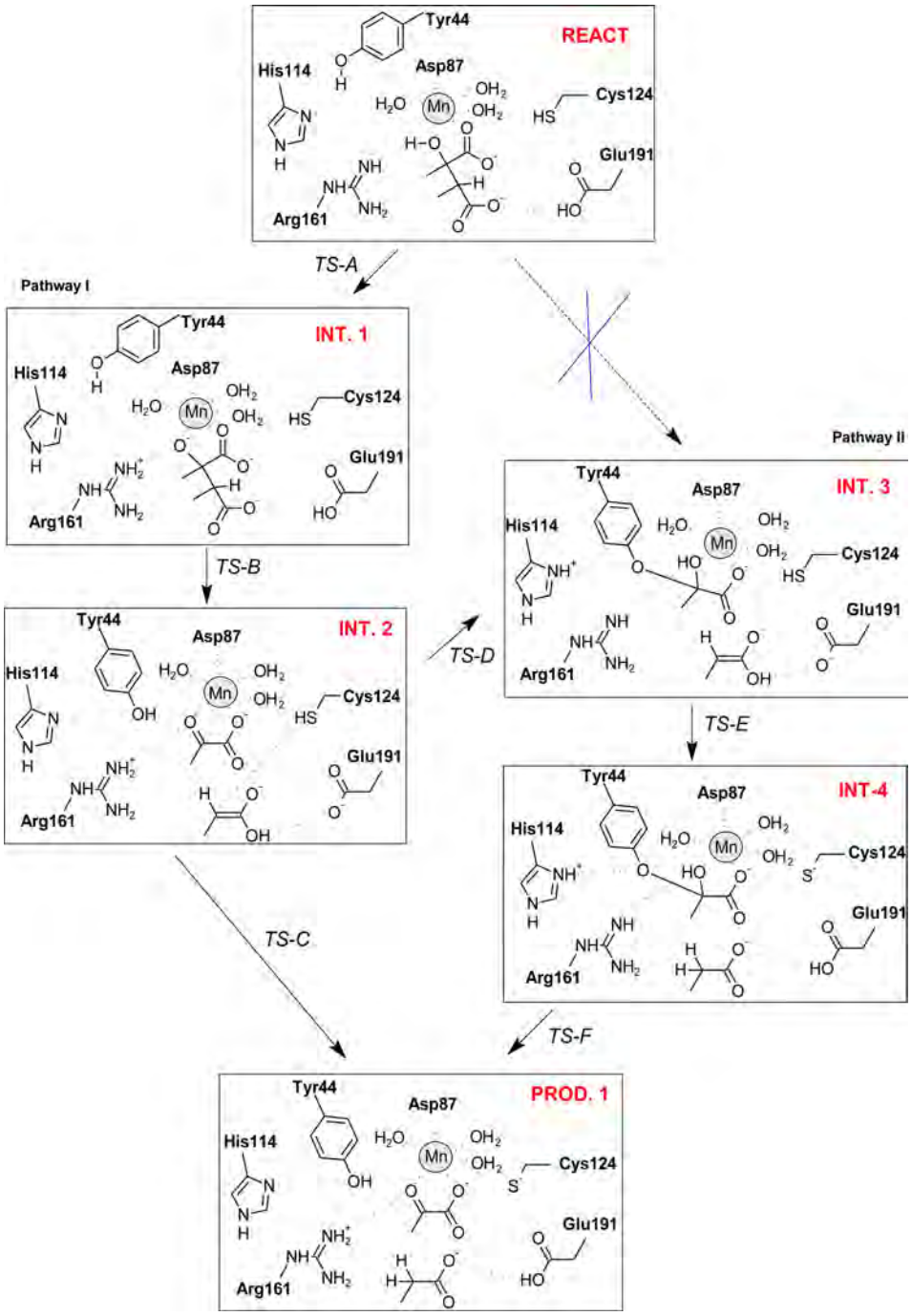

also suggests one exists in the deprotonated state. The substrate hydroxyl group was therefore deprotonated in the initial MM model.

2.1. Molecular Dynamics Simulations. Molecular dynamics (MD) of the DMML complex involved equilibrating the system with 1 ns of restrained molecular dynamics, using a protocol described in detail elsewhere,[45] to produce the starting structure for QM/MM simulations. Molecular mechanics optimizations and dynamics simulations were performed with the Gromacs program v4.5[46] and the AMBER99SB force field.[47,48] Ligand topology files were generated by use of the ACPYPE script with the GAFF force field being specified.[49,50] The system was immersed in a cubic box of TIP3P water[51,52] with a 12 Å distance from the protein to the edge of the box (9370 water molecules in total). The system was neutralized with NaCl (0.15 M).

The MD protocol involved four distinct steps to produce a catalytically active protein conformation of reduced strain, which was then suitable for use in the subsequent QM/MM studies. In the first step, all atoms except hydrogens were restrained (harmonic restraint of 1 kcal/mol·Å^2) and the system was optimized to a root-mean-square (RMS) gradient of 10 kJ·mol^{-1}·nm^{-1}. The second step saw the model being reoptimized with the restraints remaining on the protein backbone only. The system was heated to 300 K in 100 ps, followed by 200 ps of equilibration and a 1 ns production run

DOI: 10.1021/acs.jpcb.5b04732
J. Phys. Chem. B 2015, 119, 11473−11484

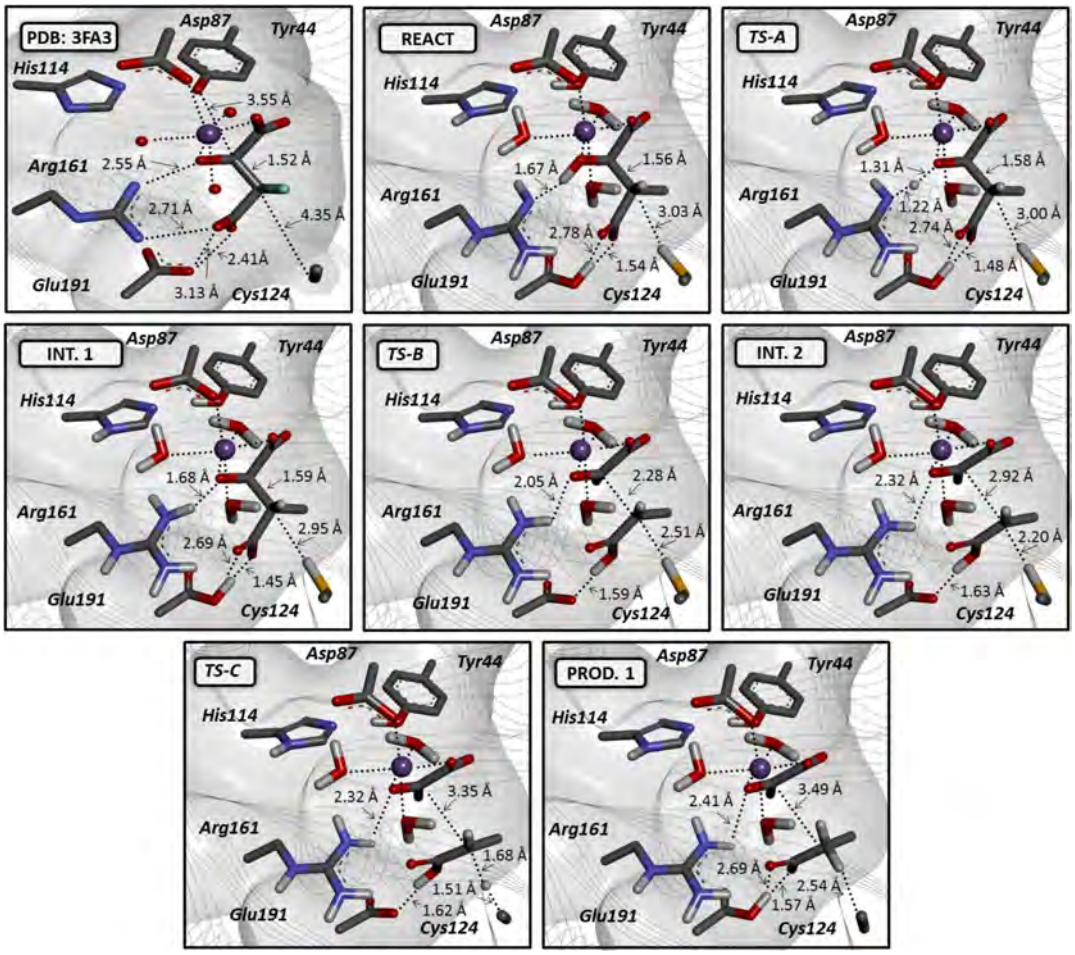

Figure 1. Graphical illustration of QM/MM stationary points associated with pathway I obtained at the M06/6-31G(d)/AMBER level of theory.

under the NPT scheme (P = 1 atm). All dynamics simulations employed a 1 nm van der Waals cutoff, the Lincs algorithm in conjunction with a 2 fs time step, the Berendsen coupling thermostat,[53] and the particle mesh Ewald method.[54]

2.2. Quantum Mechanical/Molecular Mechanical Calculations. The final structure from MD was energy-minimized before being used for the QM/MM simulations. Next, the system was truncated by removing all water molecules beyond 16 Å of the natural substrate. The QM region used in this study consisted of the side chains of six residues suggested to play a role in the catalytic mechanism: Tyr44, Asp87, His114, Cys124, Arg161, and Glu191, as shown in Figure S1 in Supporting Information. The models also included the DMM substrate, manganese (Mn^{2+}, d5 high spin), and three metal-coordinating water molecules. Only atoms within 15 Å of DMM substrate were treated flexibly during the QM/MM calculations, except for those atoms whose bonds cross the QM/MM interface.[45,55] The density functional theory (DFT) M06 functional[56,57] along with the 6-31G(d) basis set for H, C, N, O, and S atoms, and TZVP for Mn were used. The QM region consisted of 96 atoms, while the MM region contained 4316. QM/MM calculations were performed in Gaussian 09 using the ONIOM electronic embedding scheme.[58]

All structures were fully optimized at the M06/6-31G(d) level [ΔE LL (low-level)]. Minima were confirmed as having no negative frequencies, and transitions states had a single negative frequency corresponding to the expected bond-breaking/forming process under investigation. Single-point QM/MM energy calculations were performed with the 6-311+G(d,p) basis set for H, C, N, O, and S atoms and TVZP for Mn [ΔE SP-HL (single-point high-level)]. Structures identified on pathway I were also fully optimized under this scheme [ΔE HL (high-level)]. For the purpose of comparison, the QM regions of the optimized LL models were reoptimized in the gas phase where the two atoms associated with the link atom bond were fixed to keep the active site in a catalytically relevant conformation.

3. RESULTS AND DISCUSSION

The energetics associated with the DMML catalytic mechanisms proposed from experimental research (Scheme 1) were explored in detail by use of the DFT QM/MM model. We evaluated the different mechanistic sequences and the different acids and bases postulated to be involved in the C(2)−C(3) bond-breaking process. In total, nine minima were identified on the DMML potential energy surface connecting the DMM reactant and the pyruvate and propionate products. In total, six transition states were also identified (Scheme 2). These structures are found on the two postulated mechanistic pathways, which we term pathway I (Figure 1) and pathway II (Figure 2). The first pathway involves an acid−base catalytic process, while the second utilizes a tyrosine nucleophile.

The energetics associated with the catalytic reaction are summarized in Table 1 and Figure 3a. The significant negative charge on specific residues and the substrate over the course of the reaction prompted benchmark calculations to assess the

DOI: 10.1021/acs.jpcb.5b04732
J. Phys. Chem. B 2015, 119, 11473−11484

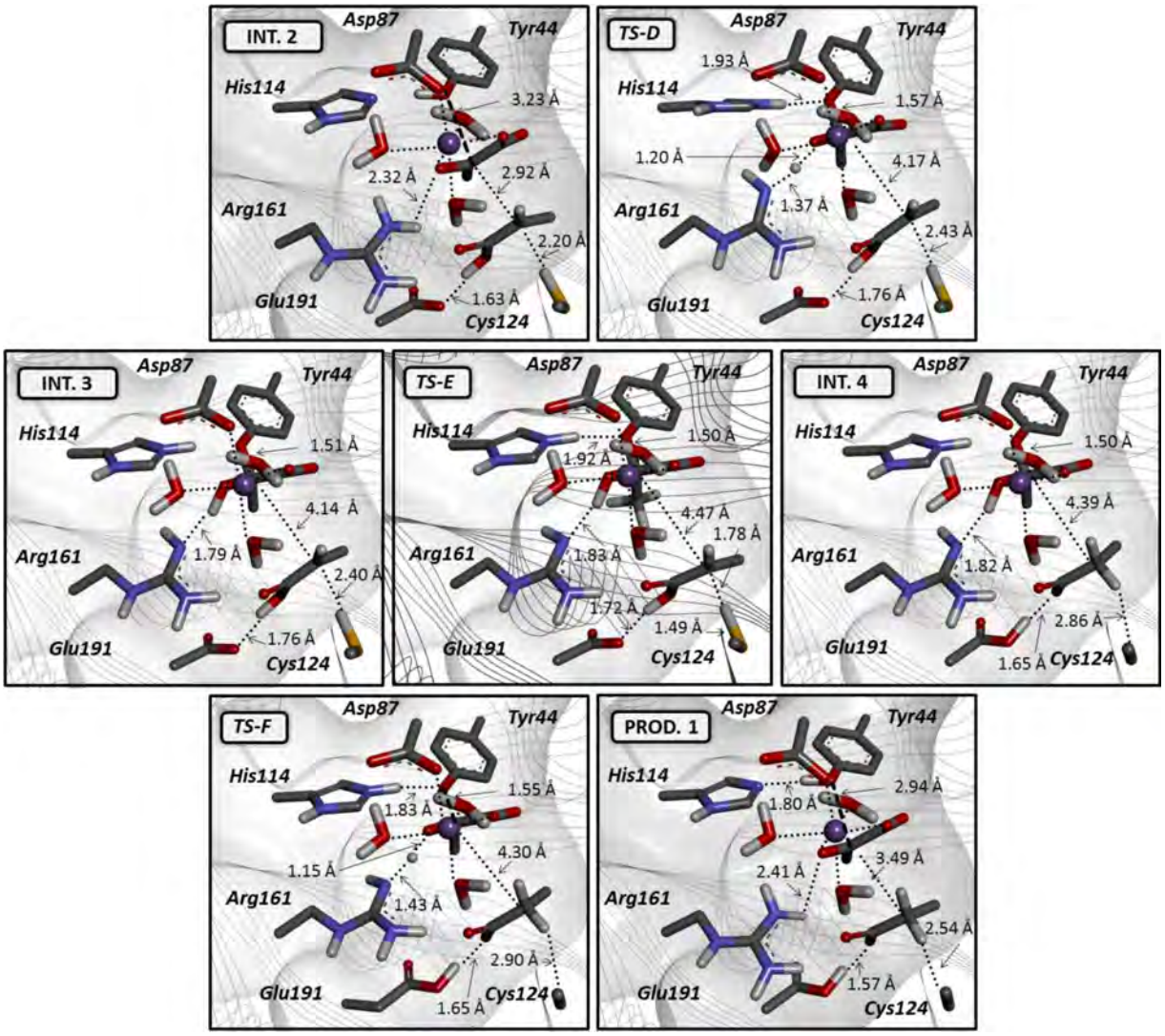

Figure 2. Graphical illustration of QM/MM stationary points associated with pathway II at the M06/6-31G(d)/AMBER level of theory.

suitability of the M06/6-31G(d):AMBER energetics (ΔE LL). Single-point energies at the M06/6-311+G(d,p):AMBER on the M06/6-31G(d):AMBER geometries were performed (ΔE SP-HL) which showed the lower level of theory to be in good overall agreement (Figure 3a). Subsequently, pathway I stationary points were fully optimized at the M06/6-311+G-(d,p):AMBER level of theory (ΔE HL) (Figure 3b) which also confirmed the results at the lower level of theory were well reflected by the latter (Figure 3c and Figure S2). Also reported are the results obtained from the QM gas-phase-based model (ΔE GP-LL). Additional energetic and geometric data are reported in the Supporting Information.

3.1. Pathway I: General Base in (2*R*,3*S*)-Dimethylmalate Lyase. We begin our discussion of the mechanism of DMML with a consideration of the reactant structure (REACT). This consists of the deprotonated Arg161 residue and the protonated substrate hydroxyl, since this is presumably the molecule that first binds to the protein from solution. Comparison of the QM/MM optimized structure to the coordinates from the X-ray crystal structure 3FA3 reveals that they are structurally very similar. The key interatomic interactions present in both systems are comparable, given the restrained MD simulation used to prepare the structure [root-mean-square deviation (RMSD) is 0.36 Å for atoms of the peptide backbone].

The active site of the metal-dependent DMML 3FA3 X-ray structure contains a Mn^{2+} cofactor in an octahedral configuration. In the X-ray crystal structure it is coordinated to three water molecules with Mn−O distances of 2.24, 2.22, and 2.35 Å. The acidic side chain of Asp87 is found to have an Mn−O distance of 2.26 Å, while the bound ligand (2,2-difluoro-3,3-dihydroxybutanedioic acid) coordinates to Mn though two oxygen-mediated interactions [O1 (hydroxyl) and O3 (carboxyl) atoms with distances of 1.98 and 1.99 Å, respectively].[1,11] Glu191 is also found to interact strongly with the bound substrate given the very short distance between the carboxylates (O---O distance <2.41 Å). This indicates that one of the residues must be protonated. Additionally, Arg161 interacts strongly with the C2 hydroxyl oxygen atom of the substrate as indicated by the corresponding N---O distance (2.55 Å). Finally, the distance between the Cys124 sulfur atom and the C(3) atom of the substrate is 4.35 Å, which is not unexpected given the nature of the moieties involved. The nearest water molecule to the substrate C(3) atom is 3.78 Å away, but it is not ideally oriented to transfer a proton upon breaking of the C(2)−C(3) bond.

DOI: 10.1021/acs.jpcb.5b04732
J. Phys. Chem. B 2015, 119, 11473−11484

Table 1. Computed QM/MM and QM Relative Energies of All Stationary Points Obtained in This Study[a]

		QM/MM model			QM model
minima	pathway	ΔE LL	ΔE SP-HL	ΔE HL	ΔE GP-LL
REACT	I	0.0	0.0	0.0	0.0
INT.1	I	0.6	−0.3	−1.5	3.6
INT.2	I	9.0	4.0	4.2	*b*
INT.3	II	68.4	61.4	62.1	59.8
INT.4	II	47.7	46.7	47.1	20.5
PROD.1	I/II	−3.2	−3.0	−3.6	9.0
PROD.2		23.1	25.7		11.3
PROD.3		18.4	17.0		9.9
PROD.4		3.5	−2.4		6.7
		QM/MM model			QM model
transition states	pathway	ΔE LL	ΔE SP-HL	ΔE HL	ΔE GP-LL
TS-A	I	3.8	2.5	2.7	
TS-B	I	11.2	6.9	7.1	
TS-C	I	11.7	8.0	8.6	
TS-D	II	71.8	66.5		
TS-E	II	71.2	65.3		
TS-F	II	49.6	48.8		

[a]QM/MM M06/6-31G(d)/AMBER (ΔE LL), single-point QM/MM M06/6-311+G(d,p)/AMBER energies on LL optimized geometries (ΔE SP-HL), and fully optimized QM/MM M06/6-311+G(d,p)/AMBER energies (ΔE HL) are given. Also reported are QM energies obtained from the gas-phase model at the M06/6-31G(d) level of theory (ΔE GP-LL). All energies are reported relative to REACT (in kilocalories per mole). [b]Unstable.

The QM/MM optimized starting structure with the modified DMM substrate [(2*R*,3*S*)-dimethylmalate, DMM] is in good overall structural agreement with the X-ray structure (Table 2). The octahedral configuration is maintained in the QM/MM model (Figure 1), with the three water molecules found to bind with Mn−O distances of 2.28, 2.25, and 2.21 Å. The interaction between Asp87 and Mn is found to be somewhat shorter than that observed in the crystal structure, with a distance of 2.06 Å, while the ligand−Mn interactions were found to be slightly longer at 2.13 and 2.16 Å for O1 and O3, respectively. This is consistent with the change from 2,2-difluoro-3,3-dihydroxybutanedioic acid to DMM. The distance between the C(2) hydroxyl substrate and the nitrogen of Arg161 is 2.67 Å, corresponding to a H-bond distance of 1.67 Å. The distance between the Glu191 carboxyl oxygen and the substrate C(3) carboxyl oxygen is found to be 2.56 Å, corresponding to a H-bond of 1.54 Å. Moreover, the distance between the Cys124 sulfur atom and the C(3) atom of the substrate is 4.27 Å, while the distance to the nearest water molecule is 3.55 Å. These correspond to C---H distances of 3.03 and 2.87 Å, respectively, although again Cys124 is in a more ideal position to transfer a proton when the C(2)−C(3) bond begins to break.

Analysis of the optimized QM/MM coordinates appears to support the role of Arg161, Glu191, and potentially Cys124 or a Mn-bound water molecule in the catalytic mechanism of DMML. The results show that a strong H-bond interaction exists involving the C(2) hydroxyl group and that Arg161 could be the key for nucleophile generation. Furthermore, the interaction between Glu191 and the C(4) carboxyl group provides a mechanism to stabilize the aci-carboxylate species generated upon C(2)−C(3) bond breaking. The QM/MM model also suggests that either Cys124 or a Mn-bound water molecule could act as the general acid in the final step of the reaction, although the latter appears preferred from geometric considerations. These aspects are now discussed in further detail.

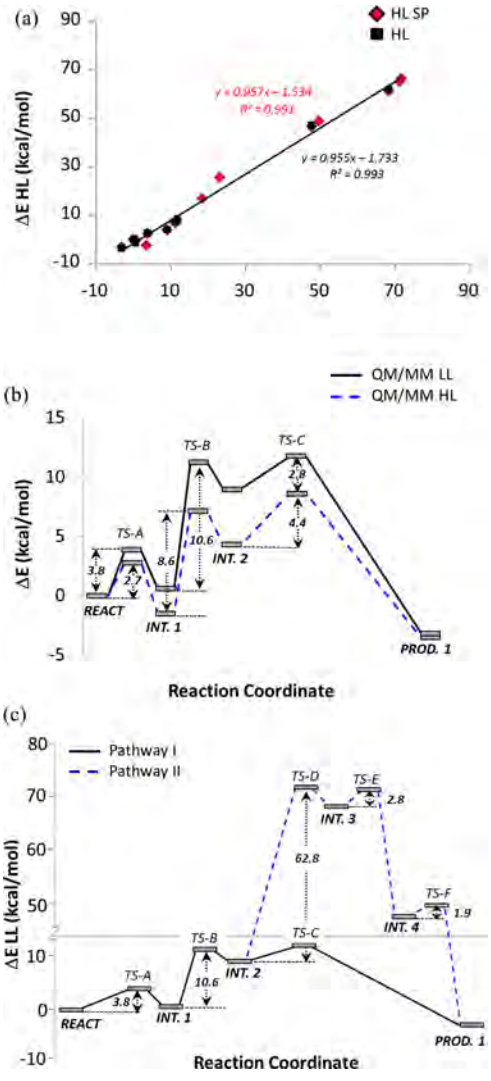

Figure 3. (a) Plot of QM/MM M06/6-31G(d)/AMBER energies (ΔE LL) vs single-point QM/MM M06/6-311+G(d,p)/AMBER energies (ΔE SP-HL). (b) Pathway I re-evaluated at M06/6-311+G(d,p)/AMBER (ΔE HL), which is shown in contrast to the ΔE LL profile. (c) Predicted QM/MM DMML profile obtained on structures optimized at the M06/6-31G(d)/AMBER level (ΔE LL).

3.1.1. Role of Arg161. It has been proposed that step 1 in the DMML reaction corresponds to activation of the substrate by abstraction of a proton. It is observed that the substrate hydroxyl group attached to the C2 atom is directly coordinated to Mn, and it is possible that the substrate could exist in either the protonated or deprotonated state, with Arg161 either having or lacking a proton as required in order to maintain the strong interaction observed in the X-ray structure. We therefore assessed the energetics associated with proton transfer. This step would generate a nucleophile with sufficient strength to form the carbonyl bond at the C(2) position and cause the ejection of the aci-carboxylate leaving group. This process could occur via ineither a stepwise or concerted fashion.

INT.1 is formed by transfer of the C(2) hydroxyl proton to the neutral arginine residue. The resulting structure retains the strong H-bond between the two groups, going from 1.67 Å in

DOI: 10.1021/acs.jpcb.5b04732
J. Phys. Chem. B 2015, 119, 11473−11484

Table 2. Key Distances Involving Pathway I[a]

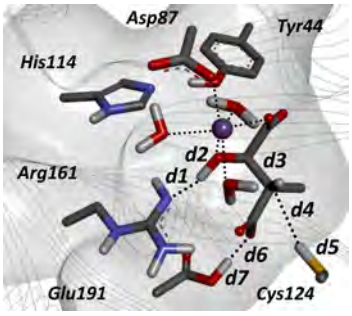

	distance						
ID	*d*1	*d*2	*d*3	*d*4	*d*5	*d*6	*d*7
X-ray			1.52				
REACT	1.67	1.02	1.56	3.03	1.35	1.54	1.03
TS-A	1.22	1.31	1.58	3.00	1.35	1.48	1.04
INT.1	1.06	1.68	1.59	2.95	1.35	1.45	1.06
TS-B	1.03	2.05	2.28	2.51	1.36	1.01	1.59
INT.2	1.03	2.32	2.92	2.20	1.39	1.06	1.63
TS-C	1.03	2.32	3.35	1.68	1.51	1.07	1.62
PROD.1	1.03	2.41	3.49	1.11	2.54	1.57	1.03

[a]Obtained from QM/MM [M06/6-31G(d)] calculation (in angstroms).

REACT to 1.68 Å in INT.1. The stationary point is found to be energetically similar to REACT at the Δ*E* HL level (−1.5 kcal/mol). The stationary point energies are found to vary subtly depending on the method used, being 0.6 kcal/mol at Δ*H* LL and −0.3 kcal/mol at Δ*E* SP-HL. Comparison of the gas-phase results to the equivalent QM/MM results shows that the protein provides additional stabilization to INT.1 by ∼3 kcal/mol. This can be rationalized on the grounds that the protein environment can better stabilize the two additional ionized moieties formed in the intermediate. Analysis of the Mulliken charge distributions in REACT and INT.1 show that Arg161 goes from 0.11 in the former to 0.79 in the latter, while the substrate goes from −1.46 to −2.03 (Table S1). The transition state connecting the two minima (i.e., TS-A) is found to be ∼2.5 kcal/mol. The transferring proton is found to be in an intermediate position between the two groups (1.22 vs 1.31 Å for Arg161 and the substrate, respectively.

We also evaluated whether one of the Mn-bound water molecules or the C(4) carboxylate of the substrate could function as the base to deprotonate the substrate hydroxyl. However, it was found that the resulting structures were unstable, decomposing to either REACT or INT.1. These results would therefore appear to confirm that Arg161 is the general base associated with the first step in the catalytic reaction.

3.1.2. Role of Glu191. Step 2, corresponding to C(2)−C(3) bond breakage, is achieved by formation of a carbonyl at the C(2) position of the substrate, leading to pyruvate as well as a highly unstable aci-carboxylate, which cannot avail itself of the stabilizing effects of the Mn^{2+} cofactor. It is observed that elongating the C(2)−C(3) bond to approximately 1.7 Å leads to transfer of a proton from Glu191 to the carboxylate group located at the substrate C(4) position (Figure 4a). The potential energy surface (PES) determined for this process shows that proton transfer from Glu191 to the substrate occurs well before TS-B is reached and results in a minimum (i.e., it is barrierless). Once the C(2)−C(3) bond extends beyond 1.7 Å, proton transfer occurs (Figure 4b), yet the transition state for step 2 is not reached until the C(2)−C(3) bond reaches 2.3 Å. It is also observed that the C(3)−cysteine distance drops dramatically upon going from INT.1 to INT.2, being 2.95 Å in the former, 2.20 Å in the latter, and 2.51 Å in the transition state. This indicates an atypical H-bond between the thiol of cysteine and the electron-rich C(3) atom of the cleaved substrate and points to it being the acid in step 3. This is further indicated by an analysis of the total Mulliken charge on the thiol, which increases from −0.02 in INT.1 to −0.09 in INT.2 (Table S1). INT.2 is found to be higher in energy than INT.1 by 8.4 kcal/mol at Δ*H* LL and to have a barrier of 10.6 kcal/mol. Due to the highly anionic nature of the stationary points, addition of diffuse functions has a noticeable effect on the energies (Δ*E* HL), giving energies for INT.2 and TS-C of 5.7 and 8.6 kcal/mol relative to INT.1, respectively.

We attempted to locate a concerted transition state whereby both proton transfer and C(2)−C(3) bond breaking occurred together. However, the PES scan in Figure 4a revealed that a concerted mechanism was not possible since both proton transfer steps are preferentially complete before extensive elongation of the C−C bond occurred (Figure 4).

3.2. Pathway I: General Acid in (2*R*,3*S*)-Dimethylmalate Lyase. The Cys124 thiol group in DMML, ICL, and related protein families is found to interact with the backbone amide of His126 (His 125 in MICL or His 193 in *Mycobacterium tuberculosis* ICL).[8,11,16,59,60] It has been proposed that this interaction should decrease the pK_a of the cysteine and aid in proton transfer to the aci-carboxylate intermediate that develops upon C(2)−C(3) bond cleavage.[11] Mutation of Cys123 to serine in MICL (Cys124 in DMML) was found to have a significant effect on its mechanism in terms of both rate and stereochemistry, adding additional evidence.[11]

3.2.1. Role of Cys124. Step 3 in the DMML reaction requires protonation of the aci-carboxylate formed in INT.2 to form propionate, the second product of the DMML catalytic reaction. The most suitable candidates for the role of general acid in the final step, based on distance and pK_a consideration, include Cys124 and a Mn^{2+}-bound water molecule. The C---HS distance between the thiol SH and the substrate in INT.2 is found to be 2.2 Å, while that for the water substrate C---HO distance is found to be 2.83 Å. In the latter case, the proton is directed toward the carboxyl group rather than the C(3) atom. Arg161 is found to be too far from the C(3) atom to contribute to the mechanism (C---HN distance of 3.04 Å). Furthermore, this residue interacts more strongly with the pyruvate molecule and is therefore an unlikely proton source.

PROD.1 is formed by the transfer of a thiol proton from Cys124 to C(3), resulting in the formation of propionate. The C(2)−C(3) distance increases further, from 2.92 Å for INT.2 to 3.49 Å for the product. The net Mulliken charge on Cys124 is −0.94, while that on the combined substrates is less negative compared to any other stationary point (−1.37) (Tables S1−S3). PROD.1 is found to be the energetically most favorable stationary point at approximately −3 kcal/mol. This is a relatively facile process due to the fact that the aci-carboxylate intermediate is rather unstable. This also provides confirmation that the C(2)−C(3) bond-breaking process (step 2) is the rate-determining step for pathway I.

Interestingly, analysis of pathway I in the gas phase showed that INT.2 did not exist, implying that the protein environment has a dramatic effect on what is the rate-determining step. The biacidic intermediate was found to be unstable, decomposing to

DOI: 10.1021/acs.jpcb.5b04732
J. Phys. Chem. B 2015, 119, 11473−11484

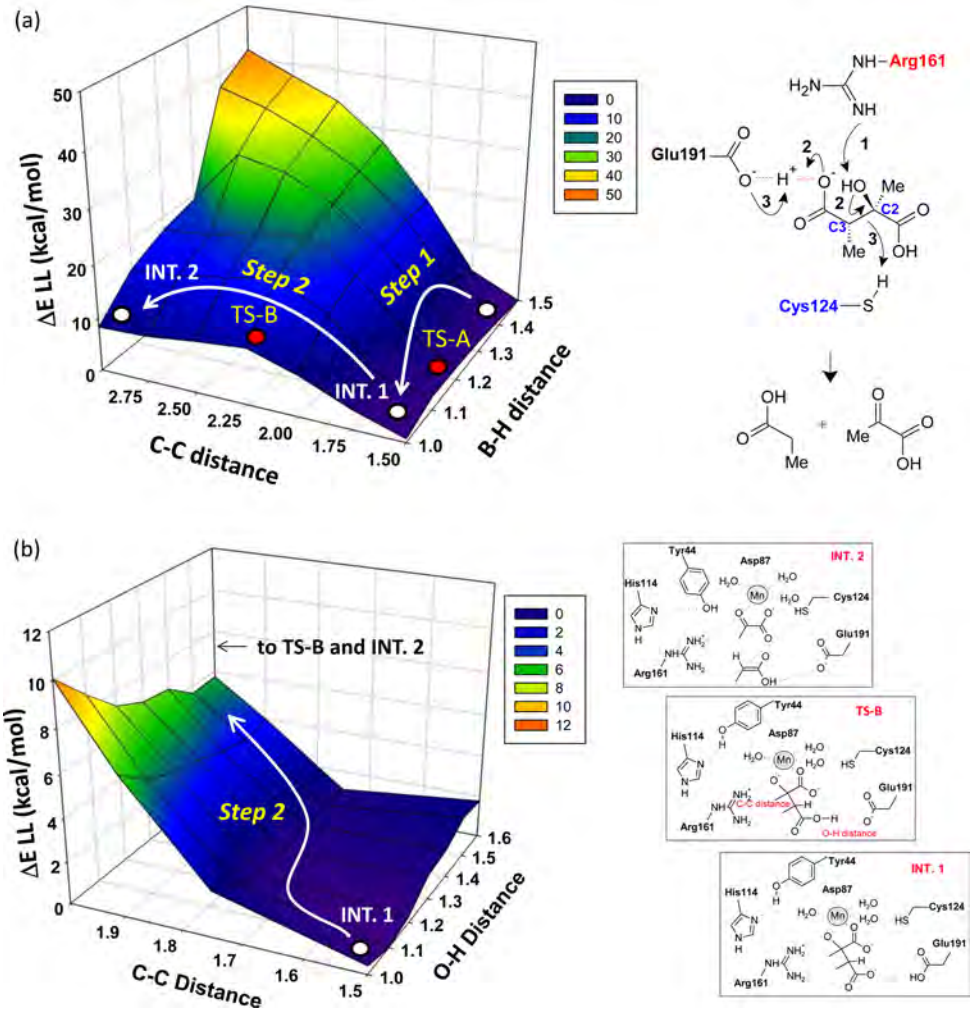

Figure 4. Potential energy surface scan describing the rate-determining step (step 2). Step 1 involves proton transfer from the C(2) hydroxyl to Arg161. Step 2 sees proton transfer to the C(4) carboxyl group from Glu191, followed by C(2)−C(3) bond breaking, which is the rate-determining step. Further analysis of proton transfer from the substrate to Arg161 (N−H distance) and subsequent C(2)−C(3) bond breaking (C−C distance) and (b) the PES around TS-B (with the N−H distance maintained at 1.0 Å) shows that proton transfer from Glu191 to the substrate upon C−C bond breakage occurs early. (a) Glu191—substrate distance was unrestrained, with proton transfer occurring spontaneously at a C−C distance of 1.7 Å and an N−H distance of 1.0 Å. (b) N−H distance is maintained at 1 Å and proton transfer is observed (C−C = 1.7 Å) before the rate-determining barrier is reached.

the corresponding INT.1 structure. Note that the gas-phase and QM/MM models were otherwise conformationally very similar (Figures S3 and S4).

3.2.2. Alternative Acid Sources. While Cys124 is in the most ideal position to transfer a proton to the aci-carboxylate intermediate corresponding to INT.2, it is possible that rearrangement could occur after PROD.1 formation. To investigate this further, we created additional product models (Figure 5 and Figure S4-S5) where the Arg161 residue was instead deprotonated (PROD.2), a Mn-bound water molecule was deprotonated (PROD.3), or the Glu191 residue was deprotonated (PROD.4). All products optimized to stable stationary points in both the QM/MM and gas-phase LL models. Interestingly, while PROD.1 and PROD.4 were found to be the most energetically favorable of the four configurations, there was no more than 5 kcal/mol difference between them in the gas phase. PROD.1 and PROD.4 were also the most stable configurations in the QM/MM model, but PROD.2 and PROD.3 were found to be approximately 15 kcal/mol higher in energy. These findings can be rationalized due to the fact that water is a less suitable acid source due to its higher pK_a. Additionally, when Arg161 and Glu191 residues are in their neutral form they have a reduced ability to stabilize the polar products of the reaction, resulting in a higher energy product. The differences between the protein and gas-phase simulations appear to be due to Asp163 and Glu116 found next to the active site region (Figure S6). In PROD.2, deprotonation of the Arg161 residue leads to a drop in the coulomb stabilization provided by these residues, while in PROD.3, deprotonation of the water molecule to give the hydroxide anion leads to an increase in electrostatic repulsion between the substrate and these residues.

From a computational analysis of the different possible acid sources in the DMML active site, it would appear that Cys124 is indeed the preferred acid in the final step of the reaction. Nevertheless, Glu191 also results in a reasonably stable product when deprotonated and may provide a mechanism whereby Cys124 can reprotonate and the newly created pyruvate and propionate can be directed out of the active site, thereby facilitating the binding of a new DMM molecule.

DOI: 10.1021/acs.jpcb.5b04732
J. Phys. Chem. B 2015, 119, 11473−11484

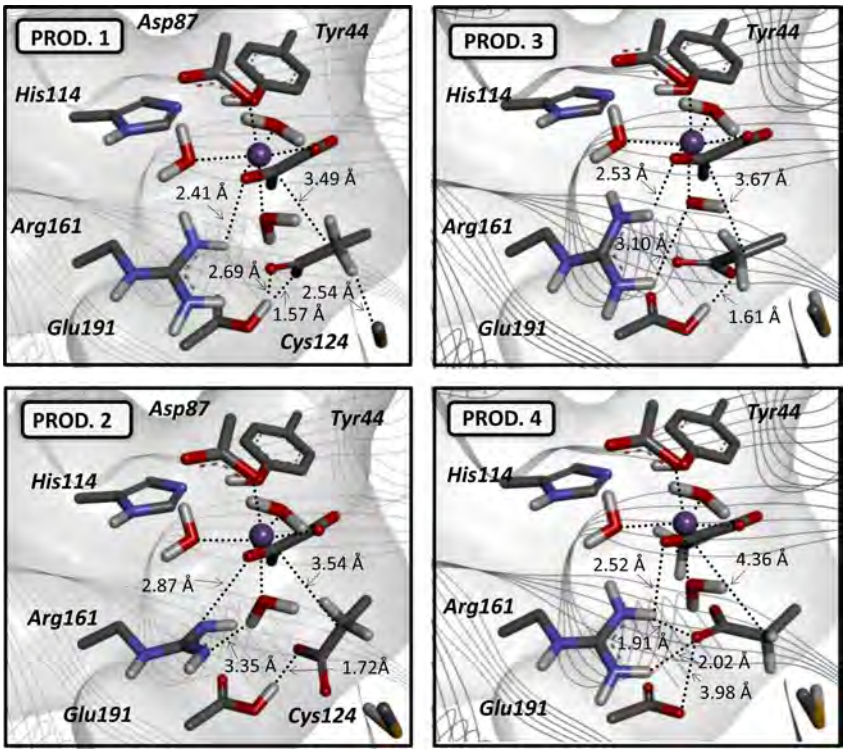

Figure 5. Four possible product configurations are possible within DMML, differing solely in terms of their protonation states.

3.3. Pathway II: Tyr44-Assisted Mechanism. It has been proposed that the C(2)−C(3) bond-breaking process could be facilitated by a mechanism involving tyrosine. In ICL (Tyr89),[11] MICL (Tyr 43),[11] and DMML (Tyr44) the Tyr−His pair may assist proton shuttling or facilitate C−C bond breakage by acting as a nucleophile to attack the C(2) position, thereby breaking the C(2)−C(3) bond by generation of the oxycarboxylate leaving group. QM/MM simulations reveal that proton transfer from Tyr44 to His114 does not result in a stable negatively charged tyrosine nucleophile. Furthermore, a concerted process whereby proton transfer is accompanied by nucleophilic attack of the substrate C(2) position also is not possible. This is because tyrosine is not a particularly strong nucleophile, nor is the resulting aci-carboxylate a good leaving group.

It is found that nucleophilic attack of a Tyr44 nucleophile occurs only once INT.2 has formed (Figure 3c). The C−O distance between the tyrosine oxygen atom decreases from 3.23 Å in INT.2 to 1.57 Å in the transition state to 1.51 Å in INT.3 (Figure 2). The corresponding substrate C(2)−C(3) distances are 2.92, 4.17 and 4.14 Å, respectively. Proton transfer from Tyr44 to His114 has already fully occurred before the transition state has been reached. The barrier to reaction is 62.8 kcal/mol (Figure 3c) and the intermediate has energy over 60 kcal/mol. The rate-determining barrier associated with the nucleophile-assisted mechanism is very high in energy since (a) histidine is not a strong base, (b) tyrosine is not a very strong nucleophile, and (c) the resultant bianionic intermediate INT.3 cannot be stabilized as effectively as the monoanionic pyruvate formed in INT.2. This finding is also consistent with the gas-phase model, which shows that INT.3 is very high in energy. This suggests that the proposed pathway does not contribute to the enzymatic activity of DMML[1] or related proteins.[11]

INT.3 can form INT.4 by proton transfer from Cys124 to the oxyacid, being analogous to TS-C. This has a barrier of just 2.8 kcal/mol and results in the formation of propionate. INT.4 is found to be approximately 45 kcal/mol higher in energy than the reactant. The final step sees proton transfer from His114 to Tyr44, leading to breaking of the Tyr−substrate C−O bond and formation of pyruvate. The barrier is just 1.9 kcal/mol for this step.

4. CONCLUSIONS

Isocitrate lyase and related enzymes are involved in metabolic pathways found in plants and microorganisms. Mechanistic proposals for the ICL superfamily have been made thus far from experimental data;[1,11,13−15] however, the precise residues involved and the sequence of events are still not resolved. In this work we have explored the possible sequences of events leading to breakage of the C−C bond of these related enzymes by focusing on DMML.

Our QM/MM calculations suggest that the most probable pathway involves three separate steps. In step 1, Arg161 acts as the general base that initiates the reaction by abstracting a proton from the C(2) hydroxyl of the substrate. This is not unsurprising since arginine residues have been implicated as a dual acid/base in several enzymatic processes including inosine 5′-monophosphate (IMP) dehydrogenase,[61,62] pectate/pectin lyases, L-aspartate oxidase,[36] tyrosine-phenol lyase,[36] citrate synthase,[35,63] and fumarate reductase.[64] Step 2 involves C(2)−C(3) bond cleavage, which is preceded by proton transfer from Glu191 to the C(4) carboxyl group (Figure 4). This is the rate-determining step with a predicted barrier of approximately 9−10 kcal/mol. The oxyacid intermediate of INT.2 is stabilized electrostatically by Glu191, while the pyruvate product is stabilized by interaction with Arg161 and by coordination to the metal cofactor. In step 3, Cys124 was identified as the general acid leading to the formation of propionate. This finding is consistent with structural studies on DMML[1] and structurally related ICL,[13] OAH,[15] and PDP.[65] An alternative

DOI: 10.1021/acs.jpcb.5b04732
J. Phys. Chem. B 2015, 119, 11473−11484

mechanistic proposal involving Tyr44 acting as a nucleophile to facilitate C−C cleavage was found to be energetically unfavorable and unlikely to contribute to the catalytic process.

It has been reported that members of the ICL superfamily could be novel targets to treat bacterial and fungal infections,[8] including tuberculosis,[9,10] due to their importance in the citric acid cycle and related catalytic pathways. Improved structural understanding of this class of proteins could prove useful in the development of novel inhibitors. Indeed, QM/MM methods such as those described herein could be useful in such efforts since the inhibitor bromopyruvate is believed to covalently attach to the catalytic cysteine residue in both MICL[60] and ICL.[16] QM/MM methods, such as that described herein, are the only methods that can take into account both chemical reactivity and protein selectivity considerations, and they could be of great utility in analogue design.

■ ASSOCIATED CONTENT

Supporting Information

The Supporting Information is available free of charge on the ACS Publications website at DOI: 10.1021/acs.jpcb.5b04732.

Illustration of DMML with the QM active site shown, reaction coordinate for conversion of DMM to pyruvate and propionate, comparison of three key minima obtained by QM/MM and QM, PROD.1−PROD.4 structures and computed gas-phase energies, and Mulliken charge distributions of DMML on pathways I and II and on PROD.1−PROD.4 (PDF)

XYZ coordinate files of INT.1−INT.4, PROD.1−PROD.4, REACT, and TS-A−TS-F (ZIP)

■ AUTHOR INFORMATION

Corresponding Author

*Phone +66-2-562-5555, ext 2210; fax +66-2-5793955; e-mail paul.gleeson@ku.ac.th.

Notes

The authors declare no competing financial interest.

■ ACKNOWLEDGMENTS

M.P.G. acknowledges financial support from Kasetsart University Research and Development Institute (KURDI) and the Thailand Research Fund (TRF), Grant RSA5700068. N.J. acknowledges financial support from the College of Industrial Technology (CIT), King Mongkut's University of Technology North Bangkok. W.C. acknowledges funding from the National Research University (NRU). We also acknowledge the use of computational resources provided by the National e-Science Infrastructure Consortium to this study (NECTEC cluster).

■ REFERENCES

(1) Narayanan, B.; Niu, W.; Joosten, H.-J.; Li, Z.; Kuipers, R. K. P.; Schaap, P. J.; Dunaway-Mariano, D.; Herzberg, O. Structure and Function of 2,3-Dimethylmalate Lyase, a PEP Mutase/Isocitrate Lyase Superfamily Member. *J. Mol. Biol.* **2009**, *386*, 486−503.

(2) Narayanan, B. C.; Niu, W.; Han, Y.; Zou, J.; Mariano, P. S.; Dunaway-Mariano, D.; Herzberg, O. Structure and Function of PA4872 from Pseudomonas aeruginosa, a Novel Class of Oxaloacetate Decarboxylase from the PEP Mutase/Isocitrate Lyase Superfamily. *Biochemistry* **2008**, *47*, 167−182.

(3) Lu, Z.; Feng, X.; Song, L.; Han, Y.; Kim, A.; Herzberg, O.; Woodson, W. R.; Martin, B. M.; Mariano, P. S.; Dunaway-Mariano, D. Diversity of Function in the Isocitrate Lyase Enzyme Superfamily: The Dianthus caryophyllus Petal Death Protein Cleaves Keto and Hydroxycarboxylic Acids. *Biochemistry* **2005**, *44*, 16365−16376.

(4) Alhapel, A.; Darley, D. J.; Wagener, N.; Eckel, E.; Elsner, N.; Pierik, A. J. Molecular and Functional Analysis of Nicotinate Catabolism in Eubacterium *barkeri*. *Proc. Natl. Acad. Sci. U. S. A.* **2006**, *103*, 12341−12346.

(5) Kung, H.-F.; Tsai, L.; Stadtman, T. C. Nicotinic Acid Metabolism: VIII. Tracer Studies on the Intermediary Roles of α-Methyleneglutarate, Methylitaconate, Dimethylmaleate, and Pyruvate. *J. Biol. Chem.* **1971**, *246*, 6444−6451.

(6) Stadtman, E. R.; Stadtman, T. C.; Pastan, I.; Smith, L. D. *Clostridium barkeri* sp. n. *J. Bacteriol.* **1972**, *110*, 758−760.

(7) Pirzer, P.; Lill, U.; Eggerer, H. Nicotinic Acid Metabolism. 2,3-Dimethylmalate Lyase. *Hoppe-Seyler's Z. Physiol. Chem.* **1979**, *360*, 1693−1702.

(8) Dunn, M. F.; Ramírez-Trujillo, J. A.; Hernández-Lucas, I. Major Roles of Isocitrate Lyase and Malate Synthase in Bacterial and Fungal Pathogenesis. *Microbiology* **2009**, *155*, 3166−3175.

(9) Lee, Y.-V.; Wahab, H. A.; Choong, Y. S. Potential Inhibitors for Isocitrate Lyase of *Mycobacterium tuberculosis* and Non-*M. tuberculosis*: A Summary. *BioMed Res. Int.* **2015**, *2015*, 895453.

(10) Muñoz-Elías, E. J.; Upton, A. M.; Cherian, J.; McKinney, J. D. Role of the Methylcitrate Cycle in Mycobacterium tuberculosis Metabolism, Intracellular Growth, and Virulence. *Mol. Microbiol.* **2006**, *60*, 1109−1122.

(11) Liu, S.; Lu, Z.; Han, Y.; Melamud, E.; Dunaway-Mariano, D.; Herzberg, O. Crystal Structures of 2-Methylisocitrate Lyase in Complex with Product and with Isocitrate Inhibitor Provide Insight into Lyase Substrate Specificity, Catalysis and Evolution. *Biochemistry* **2005**, *44*, 2949−2962.

(12) Britton, K. L.; Abeysinghe, I. S. B.; Baker, P. J.; Barynin, V.; Diehl, P.; Langridge, S. J.; McFadden, B. A.; Sedelnikova, S. E.; Stillman, T. J.; Weeradechapon, K.; Rice, D. W. The Structure and Domain Organization of *Escherichia coli* Isocitrate Lyase. *Acta Crystallogr., Sect. D: Biol. Crystallogr.* **2001**, *57*, 1209−1218.

(13) Britton, K. L.; Langridge, S. J.; Baker, P. J.; Weeradechapon, K.; Sedelnikova, S. E.; De Lucas, J. R.; Rice, D. W.; Turner, G. The Crystal Structure and Active Site Location of Isocitrate Lyase from the Fungus *Aspergillus nidulans*. *Structure* **2000**, *8*, 349−362.

(14) Grimm, C.; Evers, A.; Brock, M.; Maerker, C.; Klebe, G.; Buckel, W.; Reuter, K. Crystal Structure of 2-Methylisocitrate Lyase (PrpB) from *Escherichia coli* and Modelling of its Ligand Bound Active Centre. *J. Mol. Biol.* **2003**, *328*, 609−621.

(15) Han, Y.; Joosten, H.-J.; Niu, W.; Zhao, Z.; Mariano, P. S.; McCalman, M.; van Kan, J.; Schaap, P. J.; Dunaway-Mariano, D. Oxaloacetate Hydrolase, the C-C Bond Lyase of Oxalate Secreting Fungi. *J. Biol. Chem.* **2007**, *282*, 9581−9590.

(16) Sharma, V.; Sharma, S.; zu Bentrup, K. H.; McKinney, J. D.; Russell, D. G.; Jacobs, W. R.; Sacchettini, J. C. Structure of Isocitrate Lyase, a Persistence Factor of Mycobacterium tuberculosis. *Nat. Struct. Biol.* **2000**, *7*, 663−668.

(17) Huang, K.; Li, Z.; Jia, Y.; Dunaway-Mariano, D.; Herzberg, O. Helix Swapping between Two α/β barrels: Crystal Structure of Phosphoenolpyruvate Mutase with Bound Mg^{2+}-Oxalate. *Structure* **1999**, *7*, 539−548.

(18) Chen, C.; Sun, Q.; Narayanan, B.; Nuss, D. L.; Herzberg, O. Structure of Oxalacetate Acetylhydrolase, a Virulence Factor of the Chestnut Blight Fungus. *J. Biol. Chem.* **2010**, *285*, 26685−26696.

(19) Coincon, M.; Wang, W.; Sygusch, J.; Seah, S. Y. K. Crystal Structure of Reaction Intermediates in Pyruvate Class II Aldolase: Substrate Cleavage, Enolate Stabilization, and Substrate Specificity. *J. Biol. Chem.* **2012**, *287*, 36208−36221.

(20) Warshel, A.; Levitt, M. Theoretical Studies of Enzymic Reactions: Dielectric, Electrostatic and Steric Stabilization of the Carbonium Ion in the Reaction of Lysozyme. *J. Mol. Biol.* **1976**, *103*, 227−249.

(21) Bentzien, J.; Florian, J.; Glennon, T. M.; Warshel, A. Quantum Mechanical-Molecular Mechanical Approaches for Studying Chemical Reactions in Proteins and Solution. In *Combined Quantum Mechanical*

DOI: 10.1021/acs.jpcb.5b04732
J. Phys. Chem. B 2015, 119, 11473−11484

and Molecular Mechanical Methods; Gao, J., Thompson, M. A., Eds.; ACS Symposium Series, Vol. *712*; American Chemical Society: Washington, DC, 1998; Chapt. 2, pp 16−34; DOI: 10.1021/bk-1998-0712.ch002.
(22) Senn, H. M.; Thiel, W. QM/MM Studies of Enzymes. *Curr. Opin. Chem. Biol.* **2007**, *11*, 182−187.
(23) Brunger, A. T. Version 1.2 of the Crystallography and NMR system. *Nat. Protoc.* **2007**, *2*, 2728−2733.
(24) Sheng, X.; Liu, Y. A QM/MM Study of the Catalytic Mechanism of Nicotinamidase. *Org. Biomol. Chem.* **2014**, *12*, 1265−1277.
(25) Götz, A. W.; Clark, M. A.; Walker, R. C. An Extensible Interface for QM/MM Molecular Dynamics Simulations with AMBER. *J. Comput. Chem.* **2014**, *35*, 95−108.
(26) Mulholland, A. Chemical Accuracy in QM/MM Calculations on Enzyme-Catalysed Reactions. *Chem. Cent. J.* **2007**, *1*, 19.
(27) Shaik, S.; Cohen, S.; Wang, Y.; Chen, H.; Kumar, D.; Thiel, W. P450 Enzymes: Their Structure, Reactivity, and Selectivity-modeled by QM/MM Calculations. *Chem. Rev.* **2010**, *110*, 949−1017.
(28) Gleeson, M. P.; Hillier, I. H.; Burton, N. A. Theoretical Analysis of Peptidyl α-Ketoheterocyclic Inhibitors of Human Neutrophil Elastase: Insight into the Mechanism of Inhibition and the Application of QM/MM Calculations in Structure-Based Drug Design. *Org. Biomol. Chem.* **2004**, *2*, 2275−2280.
(29) Sirin, G. S.; Zhang, Y. How Is Acetylcholinesterase Phosphonylated by Soman? An Ab Initio QM/MM Molecular Dynamics Study. *J. Phys. Chem. A* **2014**, *118*, 9132−9139.
(30) Bowman, A. L.; Grant, I. M.; Mulholland, A. J. QM/MM Simulations Predict a Covalent Intermediate in the Hen Egg white Lysozyme Reaction with its Natural Substrate. *Chem. Commun.* **2008**, 4425−4427.
(31) Zhang, J.; Liu, Y. A QM/MM Study of the Catalytic Mechanism of Aspartate Ammonia Lyase. *J. Mol. Graphics Modell.* **2014**, *51*, 113−119.
(32) Daniels, A. D.; Campeotto, I.; van der Kamp, M. W.; Bolt, A. H.; Trinh, C. H.; Phillips, S. E. V.; Pearson, A. R.; Nelson, A.; Mulholland, A. J.; Berry, A. Reaction Mechanism of N-Acetylneuraminic Acid Lyase Revealed by a Combination of Crystallography, QM/MM Simulation, and Mutagenesis. *ACS Chem. Biol.* **2014**, *9*, 1025−1032.
(33) Su, H.; Dong, L.; Liu, Y. A QM/MM Study of the Catalytic Mechanism of α-1,4-Glucan Lyase from the Red Seaweed Gracilariopsis Lemaneiformis. *RSC Adv.* **2014**, *4*, 54398−54408.
(34) Zhu, W.; Liu, Y.; Zhang, R. A QM/MM Study of the Reaction Mechanism of (R)-Hydroxynitrile Lyases from Arabidopsis thaliana (AtHNL). *Proteins: Struct., Funct., Genet.* **2015**, *83*, 66−77.
(35) van der Kamp, M. W.; Perruccio, F.; Mulholland, A. J. High-level QM/MM Modelling Predicts an Arginine as the Acid in the Condensation Reaction Catalysed by Citrate Synthase. *Chem. Commun.* **2008**, 1874−1876.
(36) Guillen Schlippe, Y. V.; Hedstrom, L. A Twisted Base? The Role of Arginine in Enzyme-catalyzed Proton Abstractions. *Arch. Biochem. Biophys.* **2005**, *433*, 266−278.
(37) Condic-Jurkic, K.; Zipse, H.; Smith, D. M. A Compound QM/MM Procedure: Comparative Performance on a Pyruvate Formate-Lyase Model System. *J. Comput. Chem.* **2010**, *31*, 1024−1035.
(38) von Itzstein, M.; Wu, W. Y.; Kok, G. B.; Pegg, M. S.; Dyason, J. C.; Jin, B.; Van Phan, T.; Smythe, M. L.; White, H. F.; Oliver, S. W.; et al. Rational Design of Potent Sialidase-Based Inhibitors of Influenza Virus Replication. *Nature* **1993**, *363*, 418−423.
(39) Smith, A. J. T.; Zhang, X.; Leach, A. G.; Houk, K. N. Beyond Picomolar Affinities: Quantitative Aspects of Noncovalent and Covalent Binding of Drugs to Proteins. *J. Med. Chem.* **2009**, *52*, 225−233.
(40) Mah, R.; Thomas, J. R.; Shafer, C. M. Drug Discovery Considerations in the Development of Covalent Inhibitors. *Bioorg. Med. Chem. Lett.* **2014**, *24*, 33−39.
(41) Singh, J.; Petter, R. C.; Baillie, T. B.; Whitty, A. The Resurgence of Covalent Drugs. *Nat. Rev. Drug Discovery* **2011**, *10*, 307−317.
(42) Li, H.; Robertson, A. D.; Jensen, J. H. Very Fast Empirical Prediction and Rationalization of Protein pK_a Values. *Proteins: Struct., Funct., Genet.* **2005**, *61*, 704−721.
(43) Olsson, M. H. M.; Søndergaard, C. R.; Rostkowski, M.; Jensen, J. H. PROPKA3: Consistent Treatment of Internal and Surface Residues in Empirical pKa Predictions. *J. Chem. Theory Comput.* **2011**, *7*, 525−537.
(44) Søndergaard, C. R.; Olsson, M. H. M.; Rostkowski, M.; Jensen, J. H. Improved Treatment of Ligands and Coupling Effects in Empirical Calculation and Rationalization of pK_a Values. *J. Chem. Theory Comput.* **2011**, *7*, 2284−2295.
(45) Phuangsawai, O.; Hannongbua, S.; Gleeson, M. P. Elucidating the Origin of the Esterase Activity of Human Serum Albumin Using QM/MM Calculations. *J. Phys. Chem. B* **2014**, *118*, 11886−11894.
(46) Hess, B.; Kutzner, C.; van der Spoel, D.; Lindahl, E. GROMACS 4: Algorithms for Highly Efficient, Load-Balanced, and Scalable Molecular Simulation. *J. Chem. Theory Comput.* **2008**, *4*, 435−447.
(47) Hornak, V.; Abel, R.; Okur, A.; Strockbine, B.; Roitberg, A.; Simmerling, C. Comparison of Multiple Amber Force Fields and Development of Improved Protein Backbone Parameters. *Proteins: Struct., Funct., Genet.* **2006**, *65*, 712−725.
(48) Thompson, E.; DePaul, A.; Patel, S.; Sorin, E. Evaluating Molecular Mechanical Potentials for Helical Peptides and Proteins. *PLoS One* **2010**, *5*, e10056.
(49) Wang, J.; Wang, W.; Kollman, P. A.; Case, D. A. Automatic Atom Type and Bond Type Perception in Molecular Mechanical Calculations. *J. Mol. Graphics Modell.* **2006**, *25*, 247−260.
(50) Wang, J.; Wolf, R. M.; Caldwell, J. W.; Kollman, P. A.; Case, D. A. Development and Testing of a General Amber Force Field. *J. Comput. Chem.* **2004**, *25*, 1157−1174.
(51) Mark, P.; Nilsson, L. Structure and Dynamics of the TIP3P, SPC, and SPC/E Water Models at 298 K. *J. Phys. Chem. A* **2001**, *105*, 9954−9960.
(52) Price, D. J.; Brooks, C. L. A Modified TIP3P Water Potential for Simulation with Ewald Summation. *J. Chem. Phys.* **2004**, *121*, 10096−10103.
(53) Berendsen, H. J. C.; Postma, J. P. M.; van Gunsteren, W. F.; DiNola, A.; Haak, J. R. Molecular Dynamics with Coupling to an External Bath. *J. Chem. Phys.* **1984**, *81*, 3684−3690.
(54) Darden, T.; York, D.; Pedersen, L. Particle Mesh Ewald: An N log(N) Method for Ewald Sums in Large Systems. *J. Chem. Phys.* **1993**, *98*, 10089−10092.
(55) Gleeson, D.; Gleeson, M. P. Application of QM/MM and QM Methods to Investigate Histone Deacetylase 8. *MedChemComm* **2015**, *6*, 477−485.
(56) Zhao, Y.; Truhlar, D. The M06 Suite of Density Functionals for Main Group Thermochemistry, Thermochemical Kinetics, Noncovalent Interactions, Excited States, and Transition Elements: Two New Functionals and Systematic Testing of Four M06-Class Functionals and 12 Other Functionals. *Theor. Chem. Acc.* **2008**, *120*, 215−241.
(57) Valero, R.; Costa, R.; Moreira, I. P. R.; Truhlar, D. G.; Illas, F. Performance of the M06 Family of Exchange-Correlation Functionals for Predicting Magnetic Coupling in Organic and Inorganic Molecules. *J. Chem. Phys.* **2008**, *128*, 114103.
(58) Frisch, M. J.; Trucks, G. W.; Schlegel, H. B.; Scuseria, G. E.; Robb, M. A.; Cheeseman, J. R.; Scalmani, G.; Barone, V.; Mennucci, B.; Petersson, G. A.; et al. *Gaussian 09, Revision D.01*; Gaussian Inc., Wallingford, CT, 2009.
(59) Diehl, P.; McFadden, B. A. The Importance of Four Histidine Residues in Isocitrate Lyase from *Escherichia coli*. *J. Bacteriol.* **1994**, *176*, 927−931.
(60) Brock, M.; Darley, D.; Textor, S.; Buckel, W. 2-Methylisocitrate Lyases from the Bacterium *Escherichia coli* and the Filamentous Fungus Aspergillus nidulans. *Eur. J. Biochem.* **2001**, *268*, 3577−3586.
(61) Guillén Schlippe, Y. V.; Riera, T. V.; Seyedsayamdost, M. R.; Hedstrom, L. Substitution of the Conserved Arg-Tyr Dyad Selectively Disrupts the Hydrolysis Phase of the IMP Dehydrogenase Reaction. *Biochemistry* **2004**, *43*, 4511−4521.

DOI: 10.1021/acs.jpcb.5b04732
J. Phys. Chem. B 2015, 119, 11473−11484

(62) Guillén Schlippe, Y. V.; Hedstrom, L. Is Arg418 the Catalytic Base Required for the Hydrolysis Step of the IMP Dehydrogenase Reaction? *Biochemistry* **2005**, *44*, 11700−11707.
(63) van der Kamp, M. W.; Żurek, J.; Manby, F. R.; Harvey, J. N.; Mulholland, A. J. Testing High-Level QM/MM Methods for Modeling Enzyme Reactions: Acetyl-CoA Deprotonation in Citrate Synthase. *J. Phys. Chem. B* **2010**, *114*, 11303−11314.
(64) Mowat, C. G.; Moysey, R.; Miles, C. S.; Leys, D.; Doherty, M. K.; Taylor, P.; Walkinshaw, M. D.; Reid, G. A.; Chapman, S. K. Kinetic and Crystallographic Analysis of the Key Active Site Acid/Base Arginine in a Soluble Fumarate Reductase. *Biochemistry* **2001**, *40*, 12292−12298.
(65) Teplyakov, A.; Liu, S.; Lu, Z.; Howard, A.; Dunaway-Mariano, D.; Herzberg, O. Crystal Structure of the Petal Death Protein from Carnation Flower. *Biochemistry* **2005**, *44*, 16377−16384.

DOI: 10.1021/acs.jpcb.5b04732
J. Phys. Chem. B 2015, 119, 11473−11484